The Influence Of Corrosion Deposits On UO_2 Corrosion/Dissolution

D. Ofori, P.G. Keech, J.J. Noël, D.W. Shoesmith
Department of Chemistry
The University of Western Ontario,
1151 Richmond Street
London, Ontario, Canada
N6A 5B7

Abstract

The influence of acidic conditions on UO_2 fuel dissolution has been studied using electrochemical and surface analytical techniques such as Scanning Electron Microscopy (SEM) and Energy Dispersive X-ray spectroscopy (EDX). The mechanism of UO2 anodic dissolution changes for pH<5, since the solubility of U^{VI} increases substantially. Potentiostatic and Electrochemical Impedance Spectroscopy (EIS) in chloride or sulphate solutions in the pH range 0 to 3 show that the sulphate anion is more actively involved in the dissolution reaction than the chloride anion. Surface adsorption of sulphate to form an adsorbed uranyl sulphate complex appears to occur. In neutral chloride solutions containing silicate under constant current conditions (constant anodic dissolution rate), a uranyl silicate surface deposit is formed at local sites on the surface. This attributed to enhanced dissolution at these sites leading to acidic conditions underneath the deposit.

1.0 Introduction

Many advanced countries utilize nuclear reactors for electricity generation, and consequently are researching safe methods for the disposal of nuclear fuel waste produced during reactor operation. Canada's Nuclear Waste Management Organization has recommended to the federal government an Adaptive Phased Management Approach for the long-term management of used nuclear fuel, which includes centralized containment and isolation of the spent fuel in a deep geological repository, 500 to 1000 m deep in the granitic rock of the Canadian Shield [1]. In such a repository, the spent fuel, which is encased within a Zircaloy cladding [2] in the form of CANDU (CANada Deuterium Uranium) fuel bundles, would be sealed in dual-walled corrosion-resistant containers, which have an outer layer of copper and an inner layer of carbon steel, prior to emplacement in the repository. Copper is chosen for its thermodynamic stability (corrosion resistance) in anoxic environments, while the steel will provide structural rigidity.

Anoxic conditions should be rapidly established since O_2 trapped in the repository will be rapidly scavenged by reaction with either the container, oxidizable minerals or organic material present in the repository [3]. However, there exists a small probability that waste containers could fail by other processes (e.g. due to fabrication defects). Failure could lead to contact of the fuel with groundwater and the subsequent release of radionuclides. A reasonable assumption is that containment will prevent wetting of the fuel while β/γ radiation fields emanating from the fuel are significant (up to ~1000 years) [4]. Thus, the primary source of oxidants to drive fuel corrosion, and hence radionuclide release, will be the α-radiolysis of water to produce molecular oxidants such as H_2O_2 and O_2.

Unlike β or γ radiation fields, α-radiation fields decay slowly with time, and associated fuel corrosion could be sustained for a long time. Redox conditions at the fuel surface will change with time as α fields decay and oxidation of the fuel surface would be expected to cause corrosion product deposition on the surface of the fuel, leading to the following effects:

- Blockage of the fuel surface, which would reduce the exposed surface area and suppress the rate of fuel corrosion [5];
- Restriction of the diffusive mass transport of species to (e.g. H_2 from steel corrosion) and from (e.g. radiolytically produced H_2O_2) the reacting surface. This could lead to localized chemistries within pores in the deposits such as the accumulation of radiolytically-produced H_2O_2 and/or the development of localized acidity due to the hydrolysis of dissolved uranium [6];
- Co-precipitation of α-emitting radionuclides, such as ^{237}Np, thereby modifying the yield and distribution of α-radiolysis products [6].

The groundwater in the granitic rock of the Canadian Shield that may contact the fuel is expected to be near neutral to slightly alkaline (pH 5-10) with a most probable value of 8 [7-9]. UO_2 and its corrosion products are virtually insoluble in neutral to slightly alkaline aqueous media, but the solubility increases rapidly at lower pH values (below ~5) where hydrolysis of UO_2^{2+} (oxidative product of UO_2) becomes possible [10].

Santos *et al.* [11] have shown that local acidity can develop during the anodic dissolution of UO_2 electrodes, where hydrolysis of the dissolved uranyl ion,

$$UO_2^{2+} + yH_2O \rightarrow UO_2(OH)_y^{(2-y)+} + 2yH^+ \quad (1)$$

leads to the suppression of the pH at the base of the pores in corrosion product deposits or flaws in the fuel surface [12]. The development of such local conditions could lead to a more rapid release of radionuclides to the groundwater.

The primary goals of this research are: (i) to investigate UO_2 dissolution behaviour under the acidic conditions possible in pores and flaws; and, (ii) to determine the influence of fuel corrosion rate and the formation of corrosion product deposits on the establishment of acidic conditions.

2.0. Experimental Methods

2.1. Electrode pellets

Electrodes were fabricated from 1.5 at. % SIMFUEL pellets fabricated by Atomic Energy of Canada Limited (AECL) (Chalk River Laboratories, Ontario). SIMFUELs are natural UO_2 pellets doped with stable non-radioactive elements (Ba, Ce, La, Mo, Sr, Y, Zr, Rh, Pd, Ru and Nd) in appropriate proportions to mimic the chemical effects of spent fuel in CANDU reactor irradiation to 1.5 at. % burn-up [13]. The trivalent rare earth elements (RE^{3+}) substitute for U^{IV} in the UO_2 fluorite lattice, leading to an injection of holes into the 5f band and, consequently, an increase in electronic conductivity [14-16]. The noble metals (Mo, Ru, Rh, Pd) are insoluble in the oxide lattice and congregate as intermetallic particles known as ε-particles. The use of SIMFUEL provides a practical means to study fuel corrosion/dissolution without the harmful radiation fields associated with CANDU spent fuel.

2.2. Electrode preparation

2-3 mm thick discs were cut from 1.2 cm (diameter) SIMFUEL pellets using a slow speed diamond saw and made into an electrode using previously described procedure [11]. Prior to each experiment, the electrode was polished in succession with 320, 800 (if necessary) and finally 1200 grit SiC paper, and then rinsed with distilled deionized water (resistivity =18.2 MΩ·cm). The electrode was then placed in a 50:50 distilled, deionized water/methanol solution and ultrasonically cleaned for 2 min to remove any residual SiC and UO_2 debris from the electrode surface. Finally, the electrode was rinsed again with distilled deionized water.

2.3. Electrochemical Solutions

The solutions used for Electrochemical Impedance Spectroscopy (EIS) experiments were 0.1 mol·L^{-1} reagent grade NaCl (Caledon, 99.0%) (pH 1-3), and 0.1 mol·L^{-1} reagent grade Na_2SO_4 (Caledon, 99.0%) (pH 1-3). The pH was set using HCl (Caledon, 36.5-38.0%) and H_2SO_4 (Caledon, 95.0-98.0%) or NaOH (Caledon, 96.0%). For long term galvanostatic (LTG) experiments, the solution was 0.1 mol·L^{-1} Na_2SiO_3 (Alfa Aesar) + 0.1 mol·L^{-1} NaCl (Caledon, 99.0%) (pH 9.5). All solutions were prepared with distilled, deionized water (resistivity =18.2 MΩ·cm) purified using a Millipore Milli-Q-plus unit and subsequently passed through Milli-Q-plus ion exchange columns. The solution pH was monitored with an Orion pH meter (model 720A).

2.4. Electrochemical cell and equipment

All EIS experiments were conducted in a standard, three-electrode, three compartment cell with a saturated calomel electrode (SCE) reference electrode and a Pt counter electrode. For electrochemical measurements involving rotating electrodes, the disc and post electrode assembly was threaded onto the shaft of the analytical rotator (Pine Instruments Model AFASR). To prevent any unwanted metal-solution contact, the exposed rotator shaft was wrapped with ParaFilm M (PM® 996, Pechiney Plastic packaging). All electrochemical measurements were performed with a Solartron 1287 potentiostat coupled to a frequency response analyzer (FRA, Solartron 1255B). CorrWare™ software Version 2.9 (supplied by Scribner Associates) was use to control the instrument and to analyze the data.

The long term galvanostatic (LTG) experiments were performed in a single compartment electrochemical cell, containing all three electrodes. All electrochemical measurements were performed with a Solarton 1480 multistat, controlled by CorrWare™ software Version 2.9.

2.5. Experimental procedure

Figures 1 and 2 show the experimental procedures for the LTG and potentiostatic experiments. In LTG experiments, after cathodic cleaning for 10 minutes, a constant current was applied and the corresponding potential measured for periods up to 600 hours. Subsequently, the electrode was switched to open circuit and E_{corr} measured until a steady-state value was achieved followed by cathodic stripping voltammetry (CSV). Each CSV sweep started at E_{corr} and ended at -1.2V (vs. SCE). The potential scan rate was 2 mV/s. In potentiostatic experiments a series of anodic oxidations were performed, each of 10 minutes duration or until a steady state current was achieved. In these experiments the potential was increased in 25 mV increments from 150 mV to 400 mV. An EIS measurement was recorded on completion of each stage.

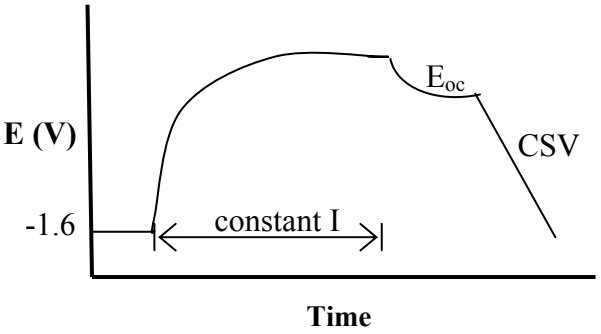

Figure 1. Experimental procedure for LTG experiments

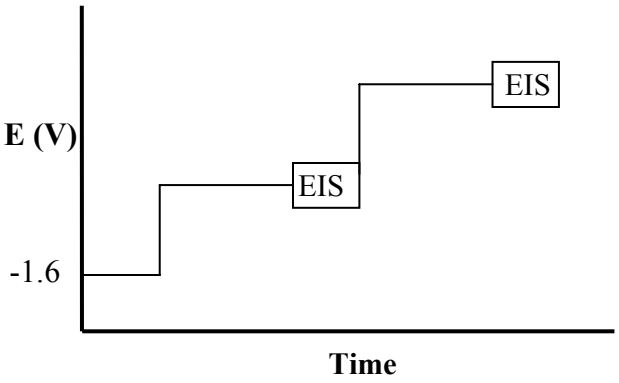

Figure 2. Experimental procedure for potentiostatic experiments

2.6. Analytical methods

Upon completion of the experiments, specimens were removed from solution, and gently rinsed with de-ionized water and examined by Scanning Electron Microscopy (SEM) and Energy Dispersive X-ray (EDX). A Hitachi S-4500 field emission SEM was used in this study.

3.0. Results and Discussion

3.1. Long Term Galvanostatic (LTG) Ex

Figure 3 shows the potential (E)-time profiles recorded for various applied anodic currents.

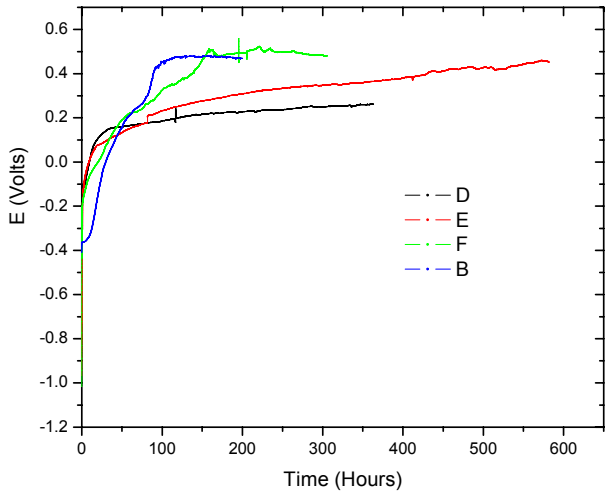

Figure 3. A potential-time profile recorded for various applied anodic current; 300 nA(blue); 100 nA (green); 20 nA (red); 10 nA (black)

The potentials for 300 nA and 100 nA eventually achieved a similar steady state potential of ~500 mV, a state achieved earlier (100 hrs.) for 300 nA than for 100 nA (150 hrs.). For 20 nA, E steadily increased and would probably have reached ~500 mV if the experiment had been longer. At 10 nA E only reached ~250 mV. Since the geometric surface area of the electrode is ~1 cm^2, applied currents can also be considered as current densities ($nA \cdot cm^{-2}$)

Figure 4 shows is a typical cyclic voltammogram recorded on SIMFUEL in $0.1 mol \cdot L^{-1}$ NaCl (pH 9.5). The numbers illustrate the stages of oxidation and reduction observed. A detailed description of the reactions occurring is given in reference [11]. This plot suggests that achieving a steady state E of 500 mV (vs. SCE), would require a current of 4×10^5 $nA \cdot cm^{-2}$. However, in the galvanostatic experiments 500 mV (vs. SCE) was achieved for 100 $nA \cdot cm^{-2}$ and possibly 20 $nA \cdot cm^{-2}$, indicating that the applied current is not evenly distributed across the electrode surface, but localized at active sites. Consequently, other surface sites must be inactive. It is also likely that active regions occur at defects located along the grain boundaries and at physical imperfections in the electrode, such as the sites of missing grains and pores.

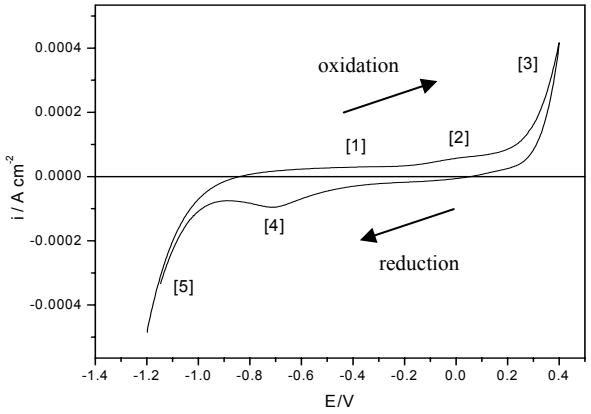

[1] oxidation of non-stoichiometric species (UO_{2+x}) up to $UO_{2.33}$
[2] oxidation of stoichiometric (UO_{2+x}) up to $UO_{2.33}$
[3] further oxidation of UO_{2+x} formed at [2] to UO_2^{2+}
[4] reduction of the anodically formed oxide
[5] reduction of H_2O to H_2 (and OH^-)

Figure 4. Voltammogram recorded on 1.5 at % of SIMFUEL at a scan rate of $10 mV \cdot s^{-1}$ in $0.1 mol \cdot L^{-1}$ NaCl (pH 9.5) [11]

Previous work by Santos *et al.* [11] concluded that at low E (-500 to +50 mV), surface oxidation of $UO_2 \rightarrow UO_{2+x}$ (mixed U^{IV}/U^{V}) occurred (regions 1 and 2 in figure 4). XPS showed that over the E range -300 mV to 0 mV, U^{V} became the dominant surface oxidation state. For the E range 0 to +400 mV (region 3 in figure 4), oxidation of $UO_{2+x} \rightarrow UO_2^{2+}$ occurs [11]. In the slightly alkaline solutions employed, the solubility of U^{VI} (as UO_2^{2+}) is very low (10^{-6} $mol \cdot L^{-1}$) [17], leading to the formation of U^{VI} deposits on the surface. In the silicate-containing solutions used in this work, these deposits are likely to be hydrated uranyl silicate [18]. Potentiostatic experiments [19] revealed that at E = +500 mV, acidity developed at local surface defect sites due to rapid uranyl ion dissolution and hydrolysis. Santos et al. [19] also showed that the accumulation of U^{VI} species on the electrode surface is a prerequisite for local acidity development, and that, at a sufficiently high concentration (similar to those used in LTG experiments) silicate suppresses the development of acidity for potentials up to 250 mV.

The measurement of E = ~ 500 mV for applied currents ≥ 20 $nA \cdot cm^{-2}$ indicates that local acidic conditions were established. However, for an applied current density of 10 $nA \cdot cm^{-2}$ the potential only reached ~ 250 mV and locally acidic sites would not be expected in our silicate-

containing solutions. However, it is possible, given time, that E measured at 10 nA·cm^{-2} may have increased further sufficiently for acidity to develop.

SEM images obtained for a current of 20 nA·cm^{-2} (i.e. $E_{steady\text{-}state}$ > 400 mV) are shown in Figure 5 (A-I).

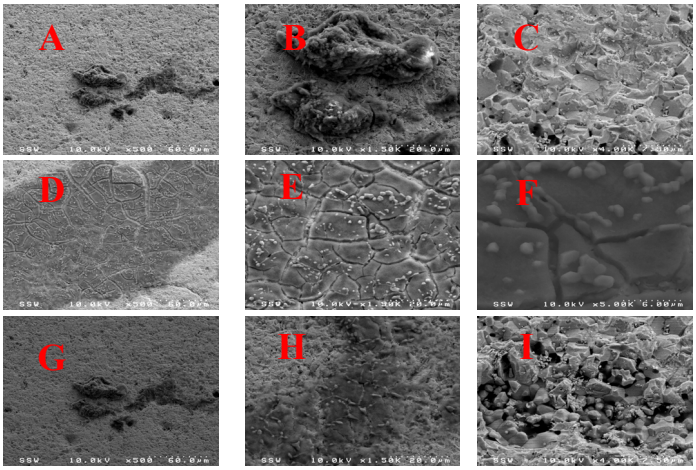

Figure 5. SEM images recorded after the completion of a 20nA galvanostatic experiment showing uranyl silicate deposits

In the images, the lighter area is the un-reacted UO_2 surface, while the dark areas have undergone dissolution as UO_2^{2+} leading to precipitation containing hydrated uranyl silicate, $UO_2(SiO_3)\cdot H_2O$. The formation of deposits occurs at only a small number of surface sites. Low magnification SEM (not shown here) revealed a total of ~ 9 sites (2-3 % coverage of the electrode surface), generally located at or around physical imperfections in the electrode. This is consistent with local current densities much greater than the applied 20 nA·cm^{-2}. Dehydration of the deposit in the SEM chamber, leads to the cracking observed.

Figure 6 show EDX maps of an area partially covered by a deposit. Figure 6A is an SEM image of the surface area over which the elemental mapping was obtained. It shows the boundary between an apparently un-reacted area of the surface (designated 1) and a deposit-covered area (designated 2) of the micrograph. The secondary electrons can be correlated to the atomic number of the element within the viewing window in the SEM, hence qualitative elemental information and the spatial distribution of elements can be revealed. The presence of uranium, silicon and oxygen, measured by EDX at the spatial location of the deposit indicates the formation of a uranyl silicate deposit. These observations are consistence with the results of Santos *et al.* [19]; i.e. the active site becomes covered with a hydrated U^{VI} silicate deposit. The EDX maps figures 6B-G also reveals that there is a higher U content coupled to a lower Si and O content on the lighter area of the electrode surface, 1 in figure 6A. This supports our claim that the lighter area on the electrode surface is un-reacted UO_2, and therefore shows no deposition of uranyl silicate. A closer look reveals that the clusters of white crystals on top of the deposit are NaCl crystals deposited from the electrolyte on removal of the electrode from the NaCl solution.

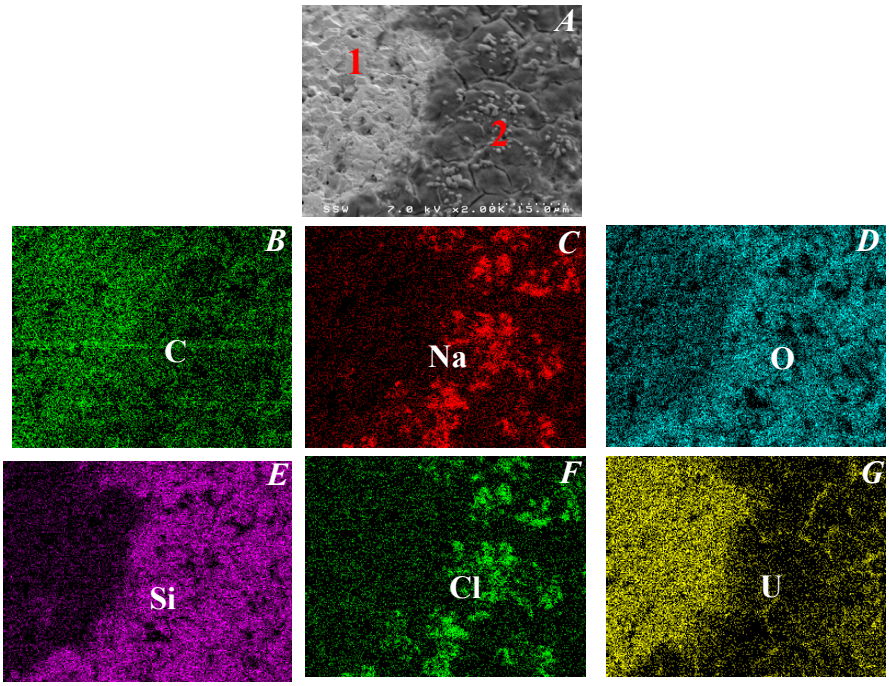

Figure 6. An SEM image and EDX maps for C, N, O, Si and U after the 20nA experiment.

The deposition of uranyl silicate maintains acidity under the deposit by preventing H^+ transport, away from the fuel surface. The extent of local acidification will control the rate of formation of UO_2^{2+}; i.e., the current densities within the sites. The growth of the observed U^{VI} deposit could continue indefinitely since UO_2^{2+} diffusing out of the site will encounter neutral to slightly alkaline conditions and precipitate. At such low general current densities only a small number of such sites can be sustained. It is not known how deep the attacked sites were. However, the SEM evidence in figure 5 indicates that the deposits spread laterally rather than penetrated deeply. If the site is spreading (i.e. increasing in area) then most of the deposit-covered area cannot continue to dissolve because this would lead to a decrease in local current density. Thus, the observed lateral spreading of the deposit indicates that only localized sites remain acidic. For these areas to spread across the surface they must be located at the edge of the deposit-covered areas.

3.2. Potentiostatic and EIS experiments in acidic solutions

Figure 7 show plots of the dissolution current vs. E in chloride and sulphate/bisulphate solutions. Both solutions exhibit similar trends: a decrease in current between 150 mV < E < 225 mV, followed by an increase for E > 250 mV. According to electrochemical theory, under steady-state conditions, there should be a linear relationship between the logarithm of the dissolution current and potential. This is known as the Tafel relationship,

$$\log I = \log I_o + \frac{\alpha n F}{RT} E \qquad (2)$$

where I is the steady-state dissolution current, I_o is the exchange current for the reaction $UO_2 \leftrightarrow UO_2^{2+} + 2e^-$, α is the transfer coefficient for the electron transfer often 0.5, F is Faraday's constant, R is the gas constant and n is the number of electrons involved in the rate determining step (rds). The slope of the Tafel plot is given by αnF/RT. A Tafel slope of 120 mV/decade of current implies

one electron is involved in the rds. If two electrons are involved in the rds then a slope of 60 mV/decade will be obtained. Other values of Tafel slope indicate more complicated mechanisms.

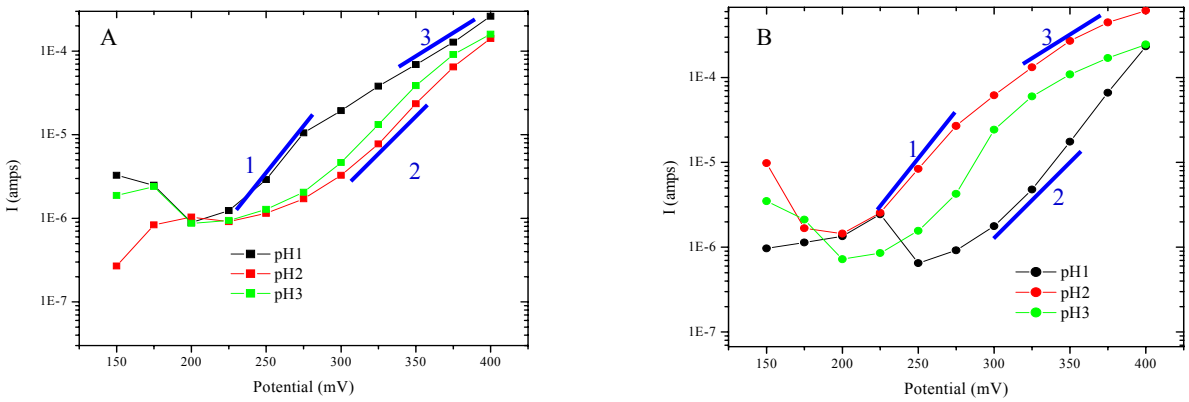

Figure 7. Dissolution currents plotted as a function of potential for (A) chloride (B) sulphate The lines show possible Tafel slopes: (1) 40 mV/decade (2) 60 mV/decade; (3) 120 mV/decade

Shown on figure 7 are three lines (labeled 1,2, and 3) indicating three possible Tafel slopes which can be derived theoretically based on the following possible mechanism suggested for the anodic dissolution of UO_2 in acidic solutions [21],

Step 1 $UO_2 + H_2O \rightleftharpoons (U^{V}O_2OH)_{ads} + H^+ + e^-$ (3)

Step 2 $(U^{V}O_2OH)_{ads} + H_2O \rightarrow (U^{VI}O_2(OH)_2)_{ads} + H^+ + e^-$ (4)

Step 3 $(U^{VI}O_2(OH)_2)_{ads} + 2H^+ \rightarrow UO_2^{2+} + 2H_2O$ (5)

Analysis of the kinetics of the above reaction schemes would yield the following Tafel slopes:

- If step 2 is the rds and step 3 occurs rapidly, then a Tafel slope of 60 mV/decade would imply a direct two electron transfer.
- If the two electron transfer reactions (steps 1 and 2) are of comparable rates then the rds would change with the applied potential.
- If the rate of the forward reaction in step 1 is slow, which is possible at lower potentials, then a slope of 40 mV/decade would be expected at low potentials. However, as the potential was increased, the rate of the forward reaction of step 1 and the rate of step 2 would both increase, while the rate of the reverse reaction of step 1 would become negligibly slow. Then a Tafel slope of 120 mV/decade would be expected at higher potentials.

A close inspection of the current-time plots reveals that steady-state was not achieved for potentials $\leq$ 200 mV. This would explain the larger than expected currents below 200 mV, and these values are not included in subsequent analyses.

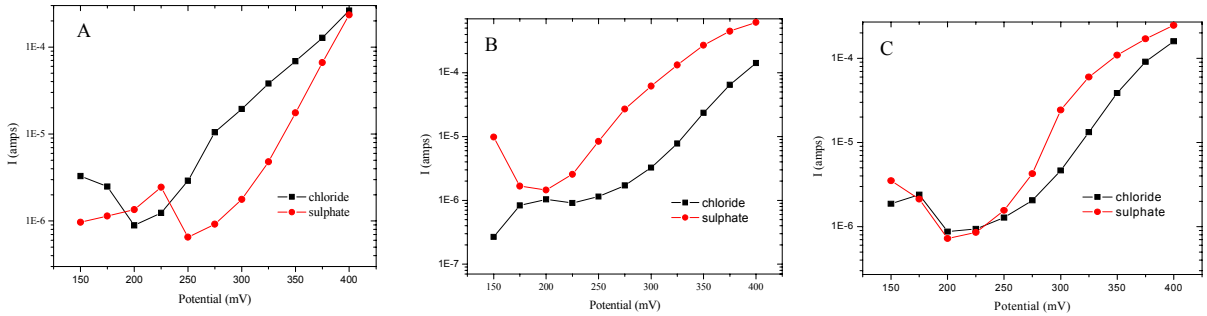

Figure 8. Dissolution current plotted as a function of potential in chloride (black) and sulphate (red) at (A) pH=1; (B) pH=2; (C) pH=3

Figure 8 shows that the influence of pH is different in chloride solutions than it is in sulphate solutions. In chloride solution the current increases as pH decreases, although the differences at pH=2 and 3 are minor. By contrast, the currents in sulphate solution were highest at pH=2 and the lowest current was observed at pH=1. This could be due to the fact that the pK_a for the protonation reaction

$$HSO_4^- \rightleftharpoons SO_4^{2-} + H^+ \quad (6)$$

is 1.7, suggesting the overall anodic dissolution reaction (the sum of equations 4, 5, and 6) is accelerated by SO_4^{2-} at pH=2 and 3 but inhibited by HSO_4^- at pH=1.

In chloride, at pH=2 and 3, the Tafel slope approaches 60mV/decade indicating a two electron transfer process. However, at pH=1, the current is significantly increased at low E and the Tafel slope changes from ~ 40 mV/decade to 120 mV/decade as E increases, suggesting that step 1 (equation 3) is accelerated at pH=1 and that the rds changes with E as described above. In sulphate solutions a Tafel slope for pH=1 is difficult to define. However, at pH=2 and 3, the Tafel slope approaches 40 mV/decade at low E and changes to ~ 120 mV/decade at higher E, indicating that the reaction is dominated by the reversibility of step 1 (equation 3) at low E but completely irreversible at higher E. Figure 8B shows that, for E > 350 mV (at pH = 2 and 3), the slope of the log i-E plot is larger than 120 mV/decade suggesting the rate of the E-independent chemical reaction (equation 5) is exerting some influence on the overall kinetics.

Figure 9 shows Bode plots recorded in 0.1 $mol \cdot L^{-1}$ chloride and in 0.1 $mol \cdot L^{-1}$ sulphate at pH=3. The impedance response for frequencies > 10^4 Hz is an artifact of cell design and is ignored when fitting the data. The impedance at the low frequency limit decreases with E, consistent with the observed increase in anodic dissolution current with E. The phase angle indicates the presence of only one time constant, and the equivalent circuit shown in figure 10 can be used to fit the data, except at low frequencies and intermediate potentials. For frequencies $\leq 10^{-2}$ Hz, the impedance decreases with frequency and the phase angle shifts to positive values; i.e. the electrode/solution interface exhibits a low frequency inductive effect. The inductive effect is best observed for the sulphate solutions in the Nyquist plots shown in figure 11 which emphasize the low frequency behaviour.

At E = 250 mV figure 11A, a single time constant equivalent circuit fits the spectrum. However, as E is increased, a low frequency inductive effect is observed (B, C, and D) and it is most obvious at 275 mV and 300 mV. Inspection of figure 7 shows this inductive effect is observed in the E region in which the Tafel plot (figure 9B) indicates a change in mechanism. At higher E $\geq$ 325 mV, the inductive effect begins to disappear again. An inductive effect suggests

that a surface intermediate is involved in accelerating (increasing the dissolution current) the overall dissolution process.

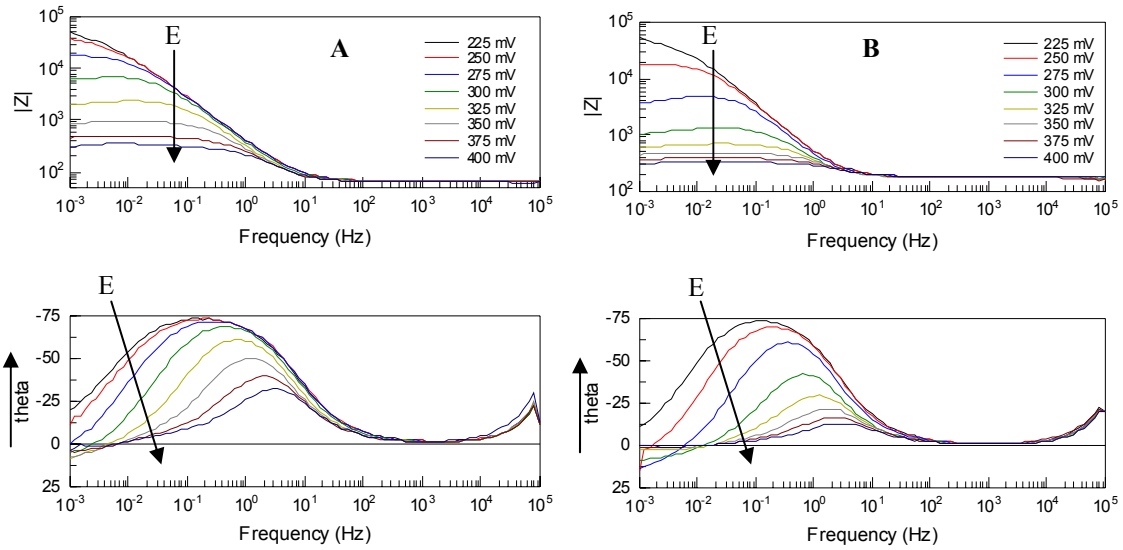

Figure 9. EIS Bode plots for 1.5 at % SIMFUEL in (A) 0.1 mol·L^{-1} NaCl, pH 3 and (B) 0.1 mol·L^{-1} Na_2SO_4, pH 3

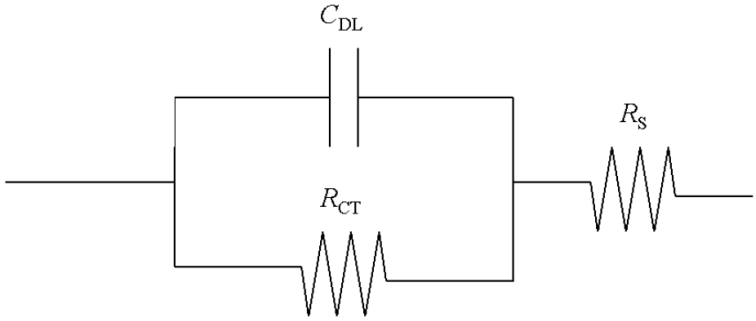

Figure 10. Simple equivalent circuit model representing a metal electrode/solution interface. R_{CT} represents the charge transfer resistance, R_S the solution resistance, and C_{DL} is the double layer capacitance.

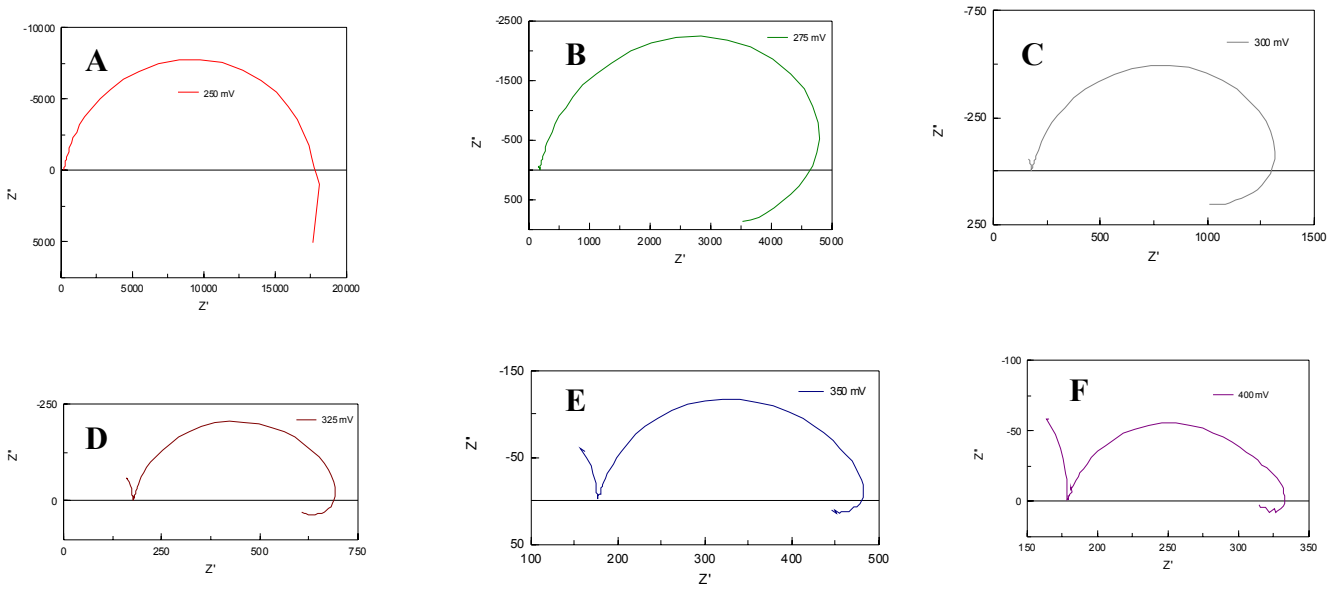

Figure 11. A series of Nyquist plots for 0.1 mol·L^{-1} Na_2SO_4 at pH=3 for (a) 250, (b) 275, (c) 300, (d) 325, (e) 350 and (f) 400 mV applied potentials.

4.0. Summary and Conclusions

In the LTG experiments, when a current density ≥ 20 nA·cm^{-2} is applied, a steady-state potential value of ~ 500 mV was achieved indicative of the development of local acidification. However the achievement of a potential of only ~ 250 mV suggests local acidification was suppressed at the lower current of 10 nA·cm^{-2}. SEM micrographs show the formation of a deposit on the electrode surface (2-3 % coverage of the electrode surface) and EDX mapping of the deposit indicates the formation of a uranyl silicate deposit.

The dissolution-current shows a difference in behaviour between chloride solutions and sulphate solutions at different pH values. EIS spectra illustrate that for frequencies ≤ 10^{-2} Hz, the impedance decreases with frequency and the phase angle reveals a low frequency inductive effect which is more pronounced in sulphate solutions. This suggests sulphate is involved as an adsorbed intermediate in the anodic dissolution process.

5.0. Acknowledgements

This research is funded under the Industrial Chair agreement between the Canadian Natural Sciences and Engineering Research Council (NSERC) and Ontario Power Generation (OPG), Toronto, Canada. We would like to thank Surface Science Western for use of their scanning electron microscope.

6.0. References

[1] Nuclear Waste Management Organization (NWMO). Choosing a Way Forward: The Future Management of Canada's Used Nuclear Fuel. Novemeber, 2005. This report is available at www.nwmo.ca.
[2] J. McMurry, D.A. Discon, J.D. Garroni, B.M. Ikeda, S. Strois-Gascoyne, P. Baumgartener, T.W. Melnyk. Ontario Power Generation Report No: 06819-REP-01200-10092-R00 (2003)
[3] L. H. Johnson, D.M. Le Neveu, F. King, D.W. Shoesmith, M. Kolar, D.W. Oscarson, S. Sander, C. Onofrei, J.L. Crosthwaithe. Atomic Energy of Canada Limited Report, AECL-11494-2, COG-95-552-2, (2000)
[4] S. Sunder. Atomic Energy of Canada Limited Report, AECL-11380, COG-95-340 (1995)
[5] D.W. Shoesmith. Journal of Nuclear Materials (2000), **282** (1), 1
[6] D.W. Shoesmith, M. Kolar, F. King. Corrosion, (2003), **59** (9), 802
[7] M. Gascoyne, Ontario Power Generation Report No: 06819-REP-01200-10033-R00 (2000)
[8] R.J. Lemire, F. Garisto, Atomic Energy of Canada Limited Report, AECL-10009 (1989)
[9] F. Garisto, A. D'Andrea, P. Gierszewski, T. Melnyk. Ontario Power Generation Report No: 06819-REP-01200-10107-R00 (2004)
[10] S. Sunder, L.K. Strandlund, D.W. Shoesmith. Electrochimica Acta, (1998), **43** (16-17), 2359
[11] B.G. Santos, J.J. Noel, D.W. Shoesmith. Electrochimica Acta (2004), **49** (11), 1863
[12] B.G. Santos, J.J. Noel, D.W. Shoesmith. Journal of Electroanalytical Chemistry (2006), **586** (1), 1
[13] P.G. Lucuta, R.A. Verrall, H. Matzke, D.S. Hartwig, in: I.J. Hastings (Ed.), Proceedings of the Second International Conference on CANDU Fuel, vol. 132, 1989
[14] G.J. Hyland, J. Ralph. High Temperatures High Pressures (1983), **15** (2), 179
[15] N.J. Dudney, R.L. Coble, H.L. Tuller. Journal of the American Ceramic Society (1981), **64** (11), 627
[16] P.W. Winter. Journal of Nuclear Materials (1989), **161** (1), 38
[17] D.W. Shoesmith, W.H. Hocking, S. Sunder, J.S. Betteridge, N.H. Miller. Journal of Alloys and Compounds (1994), **213-214,** 551
[18] M. Amme, T. Wiss, H. Thiele, P. Boulet, H. Lang. Journal of Nuclear Materials (2005), **341** (2-3), 209
[19] B.G. Santos, J.J. Noël, D.W. Shoesmith. Electrochimica Acta (2006), **51** (20), 4157
[20] B.G. Santos, J.J. Noël, D.W. Shoesmith. Corrosion Science (2006), **48** (11), 3852
[21] M.J. Nicol, C.R.S. Needes. Electrochimica Acta (1975), **20** (8), 585